Research Article Vol. 30, No. 14 / 4 Jul 2022 / Optics Express 24407
Optics EXPRESS

Size-dependent optical forces on dielectric microspheres in hollow core photonic crystal fibers

PETER SEIGO KINCAID,[1,5] ALESSANDRO PORCELLI,[1,2,5] ANTONIO ALVARO RANHA NEVES,[3] ENNIO ARIMONDO,[1,4] ANDREA CAMPOSEO,[2] DARIO PISIGNANO,[1,2] AND DONATELLA CIAMPINI[1,4,*]

[1]*Dipartimento di Fisica "E. Fermi", Université di Pisa, Largo B. Pontecorvo 3, I- 56127 Pisa, Italy*
[2]*NEST, Istituto Nanoscienze-CNR and Scuola Normale Superiore, Piazza S. Silvestro 12, I- 56127 Pisa, Italy*
[3]*Universidade Federal do ABC, Av. dos Estados 5001, Santo André, SP CEP 09210-580, Brazil*
[4]*INO-CNR, Via G. Moruzzi 1, I- 56124 Pisa, Italy*
[5]*Co-first authors with equal contribution*
[*]*donatella.ciampini@unipi.it*

Abstract: Optical forces on microspheres inside hollow core photonic crystal fibers (HC-PCFs) are often predicted using a ray optics model, which constrains its validity based on wavelength and microsphere sizes. Here, we introduce a rigorous treatment of the electromagnetic forces based on the Lorenz-Mie theory, which involves analytical determination of beam shape coefficients for the optical modes of a HC-PCF. The method is more practicable than numerical approaches and, in contrast with ray optics models, it is not limited by system size parameters. Time of flight measurements of microspheres flying through the HC-PCF lead to results consistent with the Lorenz-Mie predictions.

1. Introduction

Hollow optical waveguides offer the possibility to perform light-matter interaction experiments in a controlled environment, allowing for optical trapping and manipulation of atoms [1] and microparticles [2]. The first hollow optical waveguides were simple dielectric pipes guiding light through internal reflection. However, the higher refractive index of the cladding with respect to the hollow core determines an inherently lossy light propagation that severely limits the range of the interaction in the near infrared (NIR) and visible spectra; millimeter–sized hollow fibers feature a minimum loss of 0.17 dB m^{-1} at the wavelength of 10.6 μm [3]. This limitation was overcome with the introduction of hollow core photonic crystal fibers (HC-PCFs) as the first low-loss hollow core optical waveguides [4], which guide light by employing two-dimensional photonic crystals in the cladding of the fiber. Generally, such microstructures feature either a forbidden photonic bandgap preventing light from escaping the hollow core (also known as photonic band-gap fibers [4]) or inhibit coupling of core and cladding modes (as in the case of Kagomé structured HC-PCFs [5]). This enabled experiments at the NIR and visible wavelengths, using HC-PCFs with micron-sized cores. Recent designs featuring a hybrid photonic crystal based on Kagomé and tubular lattices had propagation losses as low as 1.6 dB km^{-1} at 1050 nm wavelength and single–mode operation [6]. Thanks to their low losses and small core sizes, HC-PCFs introduced the possibility of tight optical trapping of micro- and nano-particles in a confined environment. The mechanism for trapping and controlling these particles is generally provided by optical forces exerted by laser beams. Single–mode operation allowed for micron-sized particles to be controlled by balancing the radiation pressure and viscous forces in a liquid–filled HC-PCF

#458674 https://doi.org/10.1364/OE.458674
Journal © 2022 Received 16 Mar 2022; revised 25 May 2022; accepted 26 May 2022; published 22 Jun 2022

Optics EXPRESS

[7], whereas optical trapping and manipulation of nanoparticles were performed by generating standing wave traps with counterpropagating beams [8]. Using few-mode HC-PCFs, optical conveyor belts have been realized by exploiting the interference between co-propagating modes in the core [9], trapping of microparticle arrays has been also achieved through scattering-induced intermodal beating [10]. Recently proposed configurations for few-mode polarization maintaining HC-PCFs also predict the possibility of controlling rotational degrees of freedom of ellipsoidal microparticles [11]. The position and speed of particles trapped in HC-PCFs can be determined with high precision by non-invasive techniques, capable of measuring kinematic properties of the trapped particles: three-dimensional measurements of the particle position can be achieved with a position sensitive photodetector [8], and the velocity can be inferred through Doppler velocimetry using part of the light backscattered from the guided particle [12].

In this framework, interesting technological applications have emerged. The temperature and pressure–dependent drag forces given by fluids in the hollow core can be used for temperature sensors based on flying micro-particles [13], other sensing schemes involve rotating nanoparticle sensors of power, particle size and pressure [14] and pollution monitoring [15]. In the Mie regime of particle sizes, the interaction with the trapping laser has a strong size dependence, known as Mie resonance (also known as morphology-dependent resonance or MDR) [16,17], which has been proposed for hollow waveguide-based particle sorting or "optical chromatography" [18]. The Mie resonance can also be described in terms of the laser excitation of whispering galley modes [19,20] through which a temperature sensor application has been demonstrated using dye–doped microparticles [21]. For all these applications, determining the optical forces acting on particles trapped or flying in HC-PCFs, and understanding the role played by the particle size, is critically important. One simple approximation is based on comparing the size of the trapped particle (d) with the laser wavelength (λ). When $d/\lambda \ll 1$, the interaction is well described by Rayleigh scattering, in which the electromagnetic (EM) fields of the radiation are considered uniform across the object, whereas when $d/\lambda \gg 1$ the wavelike nature of light is neglected and the ray optics (also known as geometrical optics) approximation is applied [22]. However, for optical trapping in HC-PCF, an upper size limit for the particle diameter should be accounted for, due to the hollow core radius (order of tens of microns). Considering that the trapped particles are generally one order of magnitude smaller than the hollow core, in most cases their size falls in an intermediate regime between the two approximations ($d/\lambda \ll 1$ and $d/\lambda \gg 1$) above. It is well known that the ray optics model is inaccurate when d and λ are comparable [23]. Moreover, optical forces are more difficult to estimate in a waveguide geometry, where it is not clear that the assumptions of the standard ray-optics approach are valid [7]. Therefore, to calculate the optical forces with high accuracy, a complete treatment of the electromagnetic interactions needs to be used.

Here, the full electromagnetic calculation is performed using the generalized Lorenz-Mie theory method [24], to determine the optical forces [18,25] for dielectric particles in HC-PCFs. This approach involves finding the field expansion coefficients known as beam shape coefficients (BSCs) for the electromagnetic modes that propagate within the hollow core. This method is powerful because it allows detailed force analysis to be performed at a low computational cost, and it predicts the Mie resonances, which are expected to have a significant impact on experiments. Indeed, time-of-flight measurements using a Nd:YAG laser source (λ = 1064 nm) and polydisperse silica microspheres with 3.17 μm mean diameter in a HC-PCF, show a better agreement with Lorenz-Mie models than with ray-optics predictions.

Optics EXPRESS

2. Theoretical treatment of optical forces

2.1. Optical forces on a dielectric microsphere

The optical force exerted on a dielectric, non-absorbing microsphere, can be calculated through [26]

$$\mathbf{F} = \lim_{r\to\infty}\left[-\frac{r^2}{4}\int(\varepsilon_m|\mathbf{E}|^2 + \mu_m|\mathbf{H}|^2)\hat{\mathbf{r}}d\Omega\right], \tag{1}$$

where $\mathbf{E}$ and $\mathbf{H}$ indicate the electric and magnetic fields, and ε_m and μ_m indicate the dielectric permittivity and magnetic permeability of the medium surrounding the microsphere. In generalized Lorenz-Mie scattering theories (GLMTs), the electromagnetic fields in Eq. (1) are expressed in terms of partial wave expansions (PWEs) as follows [27]:

$$\begin{aligned}
\mathbf{E}_{\text{inc}}(\mathbf{r}) &= E_0\sum_{p=1}^{\infty}\sum_{q=-p}^{p}\left(G_{pq}^{\text{TE}}\mathbf{M}_{pq}^{(1)}(\mathbf{r}) + G_{pq}^{\text{TM}}\mathbf{N}_{pq}^{(1)}(\mathbf{r})\right)\\
\mathbf{H}_{\text{inc}}(\mathbf{r}) &= H_0\sum_{p=1}^{\infty}\sum_{q=-p}^{p}\left(G_{pq}^{\text{TM}}\mathbf{M}_{pq}^{(1)}(\mathbf{r}) - G_{pq}^{\text{TE}}\mathbf{N}_{pq}^{(1)}(\mathbf{r})\right),\\
\mathbf{E}_{\text{sca}}(\mathbf{r}) &= E_0\sum_{p=1}^{\infty}\sum_{q=-p}^{p}\left(b_{pq}\mathbf{M}_{pq}^{(3)}(\mathbf{r}) + a_{pq}\mathbf{N}_{pq}^{(3)}(\mathbf{r})\right)\\
\mathbf{H}_{\text{sca}}(\mathbf{r}) &= H_0\sum_{p=1}^{\infty}\sum_{q=-p}^{p}\left(a_{pq}\mathbf{M}_{pq}^{(3)}(\mathbf{r}) - b_{pq}\mathbf{N}_{pq}^{(3)}(\mathbf{r})\right),
\end{aligned} \tag{2}$$

where "inc" and "sca" indicate the incident and scattered electric and magnetic fields, E_0 and H_0 are the respective amplitudes, a_{pq}, b_{pq}, G_{pq}^{TE} and G_{pq}^{TM} are expansion coefficients and $\mathbf{N}$ and $\mathbf{M}$ are vector functions, defined through the relations

$$\begin{aligned}
k_m\mathbf{M}_{pq}^{(n)}(\mathbf{r}) &= i\nabla\times\mathbf{N}_{pq}^{(n)}(\mathbf{r})\\
\mathbf{N}_{pq}^{(n)}(\mathbf{r}) &= z_p^{(n)}(kr)\mathbf{X}_{pq}(\hat{\mathbf{r}})\\
\mathbf{X}_{pq}(\hat{\mathbf{r}}) &= \mathbf{L}\frac{Y_p^q(\hat{\mathbf{r}})}{\sqrt{p(p+1)}}\\
\mathbf{L} &= i\mathbf{r}\times\nabla,
\end{aligned} \tag{3}$$

where k_m is the wavenumber in the medium, Y_p^q is spherical harmonic function and $z_p^{(n)}$ is an appropriate spherical Bessel function, chosen to either be regular at the origin for the incident fields ($n = 1$), or at infinity for the scattered fields ($n = 3$).

The expansion coefficients for the incident field, G_{pq}^{TE} and G_{pq}^{TM}, are also known as BSCs, and those for the scattered field, a_{pq} and b_{pq}, are called scattering coefficients. By solving the boundary conditions for the EM fields at the surface of a microsphere with radius r_p and wavenumber k_p, the BSCs and the scattering coefficients are found to be related through the Mie coefficients, a_p and b_p, as follows [28]:

$$\begin{aligned}
a_{pq} &= -G_{pq}^{\text{TM}}\left[\frac{M\psi_p'(s)\psi_p(Ms) - \psi_p(s)\psi_p'(Ms)}{M\xi_p'(s)\psi_p(Ms) - \xi_p(s)\psi_p'(Ms)}\right] = -G_{pq}^{\text{TM}}a_p\\
b_{pq} &= -G_{pq}^{\text{TE}}\left[\frac{M\psi_p(s)\psi_p'(Ms) - \psi_p'(s)\psi_p(Ms)}{M\xi_p(s)\psi_p'(Ms) - \xi_p'(s)\psi_p(Ms)}\right] = -G_{pq}^{\text{TE}}b_p,
\end{aligned} \tag{4}$$

where ψ and ξ are Riccati-Bessel functions, $s = k_m r_p$ is the size parameter, $M = k_p/k_m$ indicates the ratio between the wavenumber inside the microsphere and in the surrounding medium. The

Optics EXPRESS

BSCs for the incident beam can be obtained through various techniques: one possible way is to manipulate the incident field expressions in Eqs. (2) to get implicit formulae for the BSCs [25]:

$$\begin{aligned} G_{pq}^{\mathrm{TM}} &= -\frac{k_m r}{j_p(k_m r)} \frac{1}{E_0\sqrt{p(p+1)}} \int Y_p^{q*}\, \hat{\mathbf{r}} \cdot \mathbf{E}_{\mathrm{inc}}(\mathbf{r}) \mathrm{d}\Omega \\ G_{pq}^{\mathrm{TE}} &= \frac{k_m r}{j_p(k_m r)} \frac{1}{H_0\sqrt{p(p+1)}} \int Y_p^{q*}\, \hat{\mathbf{r}} \cdot \mathbf{H}_{\mathrm{inc}}(\mathbf{r}) \mathrm{d}\Omega, \end{aligned} \tag{5}$$

where $j_p = z_p^{(1)}$ is a spherical Bessel function. These expressions can be determined analytically for complete solutions to Maxwell's equations, for which the apparent radial dependency cancels out [29]. By then substituting the BSC expressions in Eq. (11), we get the expansion coefficients for the scattered electromagnetic field. The force can now be calculated using Eq. (1), leading to the following expressions for the Cartesian components of the optical force, F_x, F_y, F_z:

$$\begin{aligned} \begin{bmatrix} F_x \\ F_y \end{bmatrix} &= -\frac{\varepsilon_m |E_0|^2}{(2k_m)^2} \begin{bmatrix} \mathrm{Re} \\ \mathrm{Im} \end{bmatrix} \sum_{p=1}^{\infty} \sum_{q=-p}^{p} \frac{i}{p+1} \left\{ \sqrt{\frac{p(p+2)(p+q+2)(p+q+1)}{(2p+3)(2p+1)}} \times \right. \\ &\times [A_p G_{p+1,-(q+1)}^{\mathrm{TM}} G_{p,-q}^{\mathrm{TM}*} + A_p^* G_{p,q}^{\mathrm{TM}} G_{p+1,q+1}^{\mathrm{TM}*} + B_p G_{p+1,-(q+1)}^{\mathrm{TE}} G_{p,-q}^{\mathrm{TE}*} + B_p^* G_{p,q}^{\mathrm{TE}} G_{p+1,q+1}^{\mathrm{TE}*}] + \\ &\left. - \frac{\sqrt{(p-q)(p+q+1)}}{p} [C_p G_{p,q}^{\mathrm{TM}} G_{p,q+1}^{\mathrm{TE}*} - C_p^* G_{p,q}^{\mathrm{TE}} G_{p,q+1}^{\mathrm{TM}*}] \right\} \\ F_z &= -\frac{\varepsilon_m |E_0|^2}{2k_m^2} \mathrm{Re} \sum_{p=1}^{\infty} \sum_{q=-p}^{p} \frac{i}{p+1} \left\{ \sqrt{\frac{p(p+2)(p+q+1)(p-q+1)}{(2p+1)(2p+3)}} \times \right. \\ &\left. \times [A_p G_{p+1,q}^{\mathrm{TM}} G_{p,q}^{\mathrm{TM}*} + B_p G_{p+1,q}^{\mathrm{TE}} G_{p,q}^{\mathrm{TE}*}] - \frac{q}{p} C_p G_{p,q}^{\mathrm{TM}} G_{p,q}^{\mathrm{TE}*} \right\} \end{aligned}$$

$$\begin{aligned} A_p &= a_{p+1} + a_p^* - 2a_{p+1}a_p \\ B_p &= b_{p+1} + b_p^* - 2b_{p+1}b_p \\ C_p &= a_p + b_p^* - 2a_p b_p^*. \end{aligned} \tag{6}$$

2.2. Optical modes of a HC-PCF

The exact optical modes guided in a HC-PCF can only be solved numerically, i.e. through finite element methods (FEM). However, analytical approaches are possible by employing cylindrically symmetric solutions as an approximation. The modes in HC-PCFs exhibit similar qualitative and quantitative behavior as the linearly polarized (LP) modes of an equivalent conventional solid core step-index fiber, even though the underlying physical principles are distinct [30]. Several works with PCFs use this approximation, supported by the observation of higher–order modes, such as LP_{31}, which indicates that the modal field patterns in HC-PCFs are similar to those seen in hollow capillary waveguides [31]. In addition, the cross–sectional intensity profile of the fundamental mode well fits to a Bessel squared function, which is used to describe the LP_{01} mode [32]. Another useful example in this respect is provided by measurements of the intermodal beating in HC-PCFs, where a hollow cylindrical core surrounded by a dielectric medium is considered to obtain the intermodal beat-length [9]. Given this strong evidence, we adopt the hollow cylindrical dielectric waveguide modes as the modes for our HC-PCF.

The general solutions to Maxwell's equations in cylindrical coordinates (ρ, ϕ, z), with the z–axis oriented as in Fig. 1, comprise transverse electric (TE), transverse magnetic (TM) and

Optics EXPRESS

hybrid (EH/HE) modes. Defining the two vector functions

$$\begin{aligned}\mathbf{A}_{mn}(\rho) &= iJ'_m(\chi_{mn}\rho)\hat{\rho} - \frac{mJ_p(\chi_{mn}\rho)}{\chi_{mn}\rho}\hat{\phi} \\ \mathbf{B}_{mn}(\rho) &= \frac{mJ_m(\chi_{mn}\rho)}{\chi_{mn}\rho}\hat{\rho} + iJ'_m(\chi_{mn}\rho)\hat{\phi},\end{aligned} \tag{7}$$

where J_m is the cylindrical Bessel function and χ_{mn} indicates the transverse component of k_m, we can write the expressions for TM_{mn} modes as [23]

$$\begin{aligned}\mathbf{E}^{+\mathrm{TM}}_{mn} &= E_0\left[\frac{\beta_{mn}}{\chi_{mn}}\mathbf{A}_{mn}(\rho) + J_m(\chi_{mn}\rho)\hat{z}\right]e^{i(m\phi+\beta_{mn}z)} \\ \mathbf{H}^{+\mathrm{TM}}_{mn} &= H_0\frac{k_m}{\chi_{mn}}\mathbf{B}_{mn}(\rho)e^{i(m\phi+\beta_{mn}z)},\end{aligned} \tag{8}$$

and the expressions for TE_{mn} modes as

$$\begin{aligned}\mathbf{E}^{+\mathrm{TE}}_{mn} &= -E_0\frac{k_m}{\chi_{mn}}\mathbf{B}_{mn}(\rho)e^{i(m\phi+\beta_{mn}z)} \\ \mathbf{H}^{+\mathrm{TE}}_{mn} &= H_0\left[\frac{\beta_{mn}}{\chi_{mn}}\mathbf{A}_{mn}(\rho) + J_m(\chi_{mn}\rho)\hat{z}\right]e^{i(m\phi+\beta_{mn}z)},\end{aligned} \tag{9}$$

where the + sign is used to indicate a dependency on $e^{+im\phi}$, and β_{mn} indicates the longitudinal component of k_m (also known as the propagation constant of the mode). The expressions for the hybrid modes are obtained through a superposition of the TM and TE fields in Eqs. (8) and (9), the intensity and polarization profiles of the first four cylindrical vector modes are shown in Fig. 2.

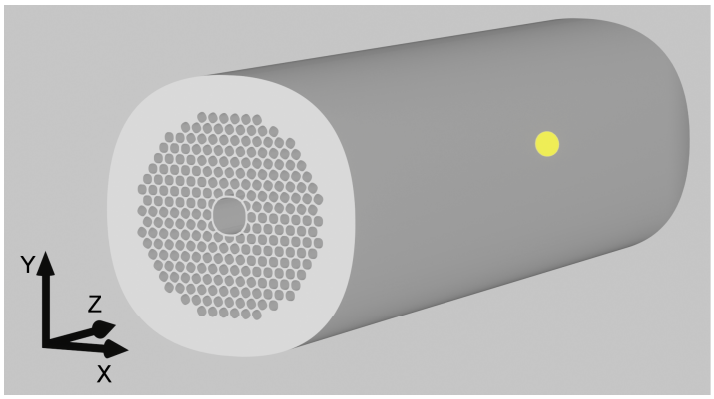

Fig. 1. Scheme of a HC-PCF with a microsphere trapped inside it (yellow sphere).

2.3. Optical forces in HC-PCF: Lorenz-Mie model

By substituting the expressions in Eqs. (8) and (9) into the integral formulae for the BSCs in Eq. (13), we can explicitly calculate G^{TE}_{pq} and G^{TM}_{pq} for both TE_{mn} and TM_{mn} modes. To avoid confusion, we will indicate the cylindrical modes in square brackets, with the plus sign indicating the dependency on $e^{+im\phi}$ and the minus sign the dependency on $e^{-im\phi}$ in the field expressions. In

Optics EXPRESS

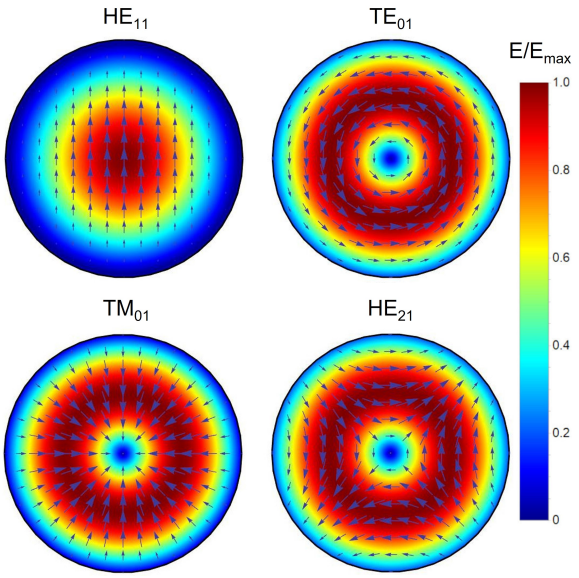

Fig. 2. The spatial profile of the electric field of the first few cylindrical vector modes propagating in a dielectric waveguide. The normalized amplitude of the electric field, $E/E_{\max}$, is represented in pseudo-colors, whereas the arrows indicate the polarization profile. The condition of null field at the core boundary is applied.

the reference frame of a sphere centered in coordinates (ρ_0, ϕ_0, z_0) with respect to the fiber axis, the beam shape coefficients for $+\mathrm{TM}_{mn}$ cylindrical modes are

$$\begin{aligned} G_{pq}^{\mathrm{TM}}[+\mathrm{TM}] &= \sqrt{4\pi} i^{p-q+1} \frac{\partial Y_p^{q*}(\alpha, \phi_0)}{\partial \cos\alpha} J_{q-m}(\chi_{mn}\rho_0) e^{im\phi_0} e^{-i\beta_{mn}z_0} \\ G_{pq}^{\mathrm{TE}}[+\mathrm{TM}] &= \sqrt{4\pi} i^{p-q} \frac{q k_m^2}{\chi_{mn}^2} Y_p^{q*}(\alpha, \phi_0) J_{q-m}(\chi_{mn}\rho_0) e^{im\phi_0} e^{-i\beta_{mn}z_0}, \end{aligned} \tag{10}$$

in which $\cos\alpha = \frac{\beta_{mn}}{k_m}$ is the ratio between the propagation constant and the wavenumber inside the core. The beam shape coefficients for the $-\mathrm{TM}_{mn}$ modes are obtained through the relation

$$G_{pq}^{\mathrm{TE/TM}}[-\mathrm{TM}] = (-1)^m G_{pq}^{\mathrm{TE/TM}}[+\mathrm{TM}]. \tag{11}$$

By directly comparing the electric and magnetic fields for the TE modes to the TM modes in Eqs. (8) and (9), we can deduce the beam shape coefficients for the TE_{mn} modes as

$$\begin{aligned} G_{pq}^{\mathrm{TM}}[\pm\mathrm{TE}] &= G_{pq}^{\mathrm{TE}}[\pm\mathrm{TM}] \\ G_{pq}^{\mathrm{TE}}[\pm\mathrm{TE}] &= -G_{pq}^{\mathrm{TM}}[\pm\mathrm{TM}]. \end{aligned} \tag{12}$$

The beam shape coefficients for hybrid modes can be obtained through linear combinations of the TE and TM expressions. Once the BSCs have been determined, the scattering coefficients can also be obtained through Eq. (11), and the resulting force on the sphere can be calculated using Eq. (1).

Optics EXPRESS

2.4. Optical forces in HC-PCF: ray optics model

Ray optics generally works when particle sizes are a lot larger than the wavelength of light used. The optical force **F** exerted on a microsphere is given by [22,33]

$$\begin{aligned}\mathbf{F} &= \frac{n_m P}{c}\boldsymbol{\eta} \\ \boldsymbol{\eta} &= \frac{1}{P}\int_S \mathbf{q}(x,y)I(x,y,z)\mathrm{d}x\mathrm{d}y,\end{aligned} \tag{13}$$

where n_m is the refractive index of the medium, the beam has power P and intensity profile $I(x, y, z)$, $\boldsymbol{\eta}$ is the total momentum transfer efficiency, integrated over the microsphere cross-section (S), and $\mathbf{q}(x, y)$ is the local momentum transfer efficiency. The transverse and longitudinal components of $\mathbf{q}$, denoted as q_ρ and q_z respectively, are a function of the incident angle θ_i and refracted angle θ_r at the medium-microsphere interface, as well as the Fresnel coefficients R and T: [22]

$$\begin{aligned}q_\rho &= R\sin(2\theta_i) - T^2\frac{\sin(2\theta_i - 2\theta_r) + R\sin(2\theta_i)}{1 + R^2 + 2R\cos(2\theta_r)} \\ q_z &= R\cos(2\theta_i) + 1 - T^2\frac{\cos(2\theta_i - 2\theta_r) + R\cos(2\theta_i)}{1 + R^2 + 2R\cos(2\theta_r)}.\end{aligned} \tag{14}$$

This method has been used in other studies [9] to describe the optical forces on a microsphere inside a HC-PCF.

2.5. Mie resonances

When compared to Rayleigh scattering or the ray optics regime, one feature of Mie scattering is strikingly different: a strong dependency of the interaction on the size parameter (s), as well as on the refractive index of the scatterer n_p. Mie resonances can be characterized through the scattering efficiency parameter, Q_{sca}, which is related to the Mie coefficients a_p and b_p through the equation [28]

$$Q_{\mathrm{sca}} = \frac{2}{s^2}\sum_{p=1}^{\infty}(2p+1)(|a_p|^2 + |b_p|^2). \tag{15}$$

Another important parameter in Mie scattering is the extinction efficiency, Q_{ext}, defined as

$$Q_{\mathrm{ext}} = \frac{2}{s^2}\sum_{p=1}^{\infty}(2p+1)\,\mathrm{Re}(a_p + b_p), \tag{16}$$

which indicates how much of the beam intensity is lost after the scattering. If the scatterer is absorbing, the absorption efficiency is then defined as $Q_{\mathrm{abs}} = Q_{\mathrm{ext}} - Q_{\mathrm{sca}}$. Upon determining analytically the BSCs of cylindrical waveguide modes, it is possible to efficiently calculate the Mie resonances excited by such modes on a dielectric microsphere. The scattering efficiency in Eq. (15) can be computed from a_p and b_p separately, as the two coefficients describe the multipole expansion of orthogonal vector spherical harmonics: those are the TM and TE spherical modes, respectively. While the Mie resonances are determined by the size parameter and the refractive index contrast, the amplitude and polarization profiles of the beams are important to determine which of these resonances are excited in a specific configuration.

3. Radiation pressure from a fundamental mode beam

The simplest configuration one can consider is that of a single beam propagating in the core of a single mode HC-PCF, pushing a flying dielectric microsphere along the fiber axis. The resulting

Optics EXPRESS

mode profile can be faithfully represented by HE_{11} in Fig. 2. A comparison between the expected radiation pressure force, F_z, obtained from Mie scattering and the ray optics approximation is shown in Fig. 3(a), for a silica microsphere ($n_p = 1.45$) pushed along an air-filled HC-PCF of core radius $a = 4.7$ μm by a 50 mW laser at 1064 nm wavelength: results from the two models get closer at high microsphere sizes, though Mie scattering reveals a complex dependency of the force on the size of the scatterer.

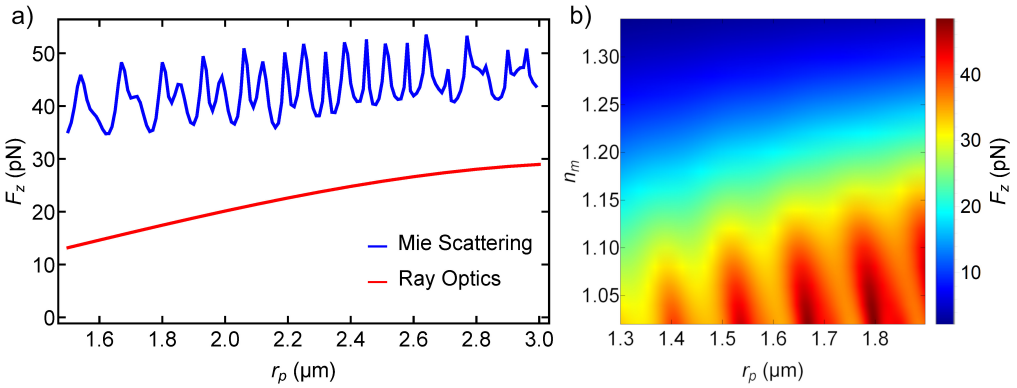

Fig. 3. (a) Calculated radiation pressure force, F_z, exerted on silica microspheres of different radii as computed through the ray optics approximation (red curve) and through Mie scattering (blue curve). (b) F_z, represented in pseudo colors, exerted on a silica microspheres of different sizes in a medium of varying refractive index, n_m. $P = 50$ mW, $\lambda = 1064$ nm, $a = 4.7$ μm, $n_p = 1.45$.

Upon analyzing this system for varying refractive indexes of the medium inside the hollow core, n_m, we find that as n_m increases the radiation pressure on the microsphere generally decreases, due to the reduction of the refractive index contrast n_p/n_m, with the pattern of maxima shifting towards smaller particle sizes (Fig. 3(b)).

By investigating systems with higher size parameters and a HC-PCF with larger core diameter, we find that the resonant peaks become more narrow; this behavior has been predicted for plane wave scattering in [34]. Highlighting the narrowest peaks in these complex patterns require a very high resolution for the size parameter: an example is reported in Fig. 4, in which a system of size parameter s>60 is analyzed with different resolutions, showing that increments in the particle radius as fine as $\Delta r_p = 2 \times 10^{-2}$ nm ($\Delta s \approx 10^{-4}$) are necessary to unveil very narrow features in the radiation pressure profile. It is worth noting that these computations can also be performed for non-spherical particles through T-Matrix formalism [35]: in the case of oblate or prolate spheroids, the high Q resonances such as the ones reported in Fig. 4 split due to the breaking of spherical symmetry [36].

Optics EXPRESS

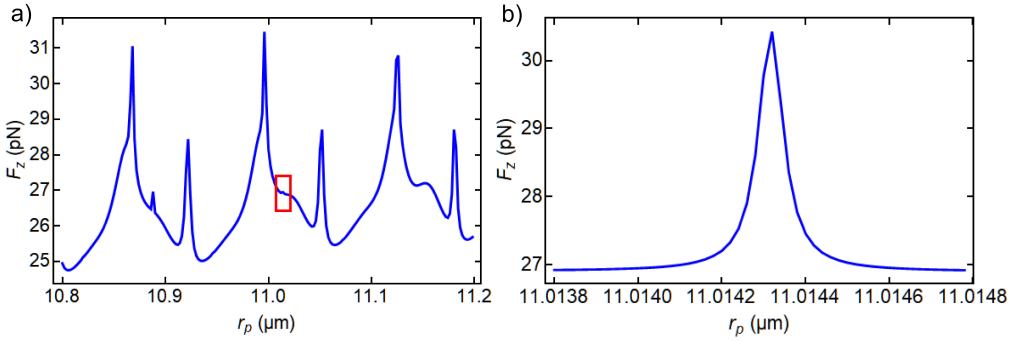

Fig. 4. Calculated radiation pressure, F_z, on silica (n_p = 1.45) microspheres of high size parameters (s>60), optically trapped in a HC-PCF of core radius a = 28 μm. (a) Data calculated with increments of the particle radius Δr_p = 2 nm. This resolution is not sufficient to highlight the narrowest resonance peaks: as an example, the region in the red rectangle has been further analyzed using increments of $\Delta r_p = 2 \times 10^{-2}$ nm revealing the presence of a narrow peak, reported in (b). P = 50 mW, λ = 1064 nm, n_m = 1, n_p = 1.45.

4. Time of flight experiments

To demonstrate the validity of our results, time of flight (t_{TOF}) measurements are performed on microspheres flying through the core of a HC-PCF at ambient temperature and atmospheric pressure, similarly to the work performed in [15]. The setup is schematized in Fig. 5(a). A 1064 nm laser beam is coupled into a HC-PCF (*HC-1060-02* by NKT Photonics) with fiber length, L = 70.4 mm using a $\lambda/2$ waveplate to optimize coupling: this is necessary due to the slight birefringence of our HC-PCF, which has been reported to be $\Delta n = 1.65 \times 10^{-4}$ [37]. The output is directed through a pinhole, to isolate the signal corresponding to the fundamental mode, and the resulting beam is focused on a photodiode after filtering. Microparticles are dispersed into distilled water and sprayed in front of the fiber end using a medical nebulizer, as in [38]. The concentration is chosen such that the average number of microparticles per droplet is less than one [10]. The recorded photodiode signal, V_{PD}, is proportional to the power in the fundamental mode, P. When a particle enters the fiber, the intensity recorded at the photodiode drops, after the particle exits it returns to its previous value, (Fig. 5(b)). The observed low frequency modulation when the particle is inside the fiber is attributed to noise, since it is not observed for all launch events; the higher frequency modulation is attributed to involuntary higher mode coupling as noted in other studies [15]. The laser power before the fiber is kept constant but the measured signal amplitude changes after each spray, due to possible contamination of optics and fiber by the aerosol, making the times of flight difficult to compare: this is mitigated by considering that the time of flight is inversely proportional to P, $t_{TOF} \propto \frac{1}{P}$. Hence we create a histogram of $t_{PD} = t_{TOF} \times \langle V_{PD} \rangle$, where $\langle V_{PD} \rangle$ is the average photodiode reading in a 0.7 second interval before each launch event (Fig. 5(b)).

We calculated the time of flight as a function of particle radius, $g(r)$, by solving the equation of motion for a spherical particle in a viscous fluid:

$$F_z - 6\pi K r \mu_{\text{air}} \dot{z}(t) = m\ddot{z}(t), \tag{17}$$

where $z(t)$ is the distance travelled by the sphere as a function of time, F_z is the radiation pressure and the second term comes from Stokes drag, in which K is the Faxén correction factor [13,39], which takes into account the additional drag force arising from confinement in a cylindrical channel, μ_{air} is the viscosity of air at ambient temperature and atmospheric pressure, and m is the mass of the sphere. The time of flight is then obtained by solving the equation of motion for

Optics EXPRESS

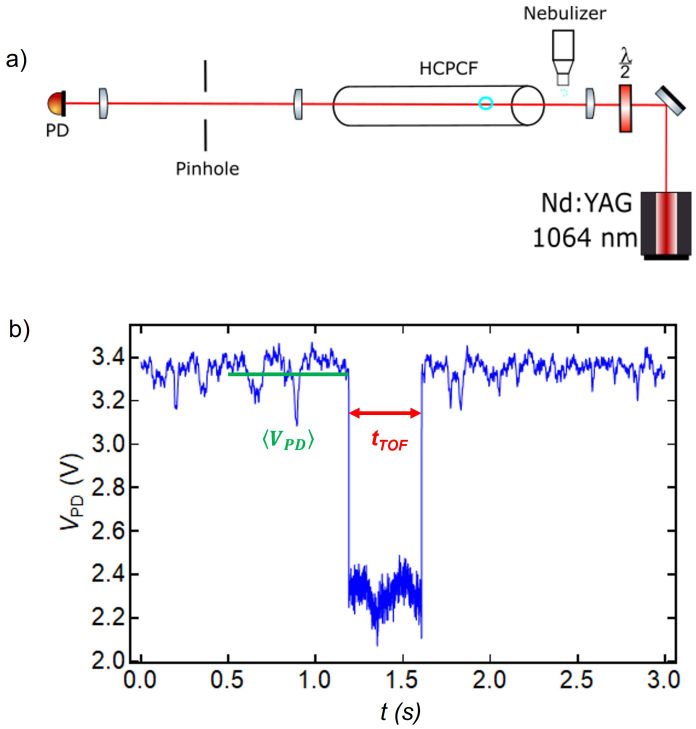

Fig. 5. (a) Schematics of the set-up used for time of flight measurements. Light from a Nd:YAG laser is directed through a $\frac{\lambda}{2}$ waveplate to optimise the orientation of linear polarisation, and it is then coupled into a fiber with a lens of focal length $f = 40$ mm. Particles are dispersed in a water solution and introduced in front of the fiber using a medical nebulizer. The light that exits the fiber is focused through a pinhole and directed to a photodiode. When a particle enters the fiber, a dip in transmitted intensity is recorded and used to measure the time of flight. (b) Example of the laser intensity signal measured by the photodiode as a function of time showing a particle launch event, occuring at $t = 1.19$ s. The width of the intensity dip is used to recover t_{TOF}, represented by the red arrow, the average photodiode reading over 0.7 s before the launch, $\langle V_{PD} \rangle$, is represented by the green line.

$z(t_{TOF}) = L$ for a range of radii to build $g(r)$, (Fig. 6(a), (c)) where the Lorenz-Mie and ray optics models were used respectively to compute the time of flight.

From Eq. (17), we see that as the particle size increases, the drag force increases proportionally, therefore increasing the time-of-flight. However, the increasing overlap of the propagating mode with the particle cross section increases the radiation pressure, decreasing the time-of-flight. In our configuration, we see that for particle radii below 1.1 micron, the radiation pressure contribution is dominant, whereas for particle sizes above 1.1 micron in radius the drag force becomes dominant.

Given the mean, 3.17 μm, and standard deviation, 0.323 μm, of the diameter of the used particles (*Bangs Laboratories*), we predict the distribution of t_{TOF} obtained by statistical analysis of the probability density function (PDF). Since in our case the time of flight is a non-monotonic function of the particle radius due to Mie resonances, the PDF of the time of flight is given by [40]

$$f_{t_{TOF}}(t_{TOF}) = \sum_{r \in g^{-1}(t_{TOF})} \frac{f_R(r)}{|g'(r)|}, \tag{18}$$

Optics EXPRESS

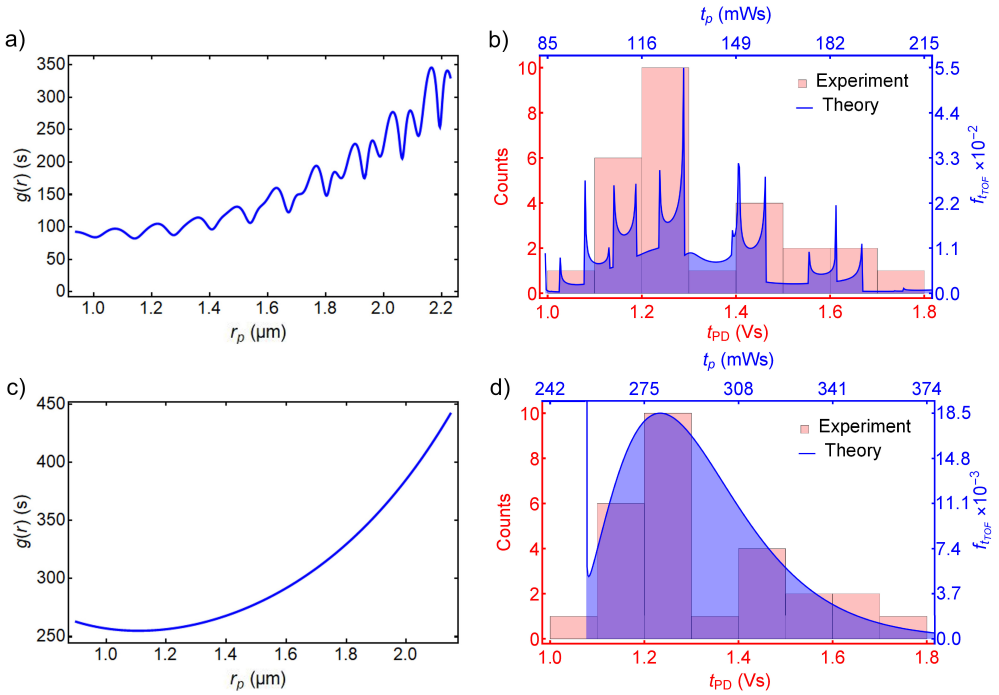

Fig. 6. Time of flight, $g(r)$, as a function of microparticle radius r_p for Lorenz-Mie (a) and ray optics (c) models, respectively, for an 8σ range around the mean value. In this range, the drag force is dominant over the radiation pressure contribution, resulting in longer times of flight for increasing particle sizes for both models. Calculations are for a 50 mW laser beam at 1064 wavelength pushing silica microspheres in a HC-PCF of core radius $a = 4.7$ μm, length 70.4 mm. Histograms of time of flight multiplied by average voltage reading on the photodiode before the launch event for 3.17 μm particles. 26 data points, 8 bins. Experimental data in pink with the theoretical probability distribution function overlayed in blue for (b) Lorenz-Mie and (d) ray optics models.

where $f_R(r)$ represents the Gaussian PDF of the microsphere radii, $g'(r)$ is the derivative of the time of flight with respect to r and $g^{-1}(t_{TOF}) = \{r : g(r) = t_{TOF}\}$. The $t_p = t_{TOF} \times P$ parameter is analysed and compared with t_{PD}. Since the predicted $g(r)$ is non monotonic, particles of different radii will have the same times of flight. However, it is still possible to infer the different particle sizes by looking at the depth of the transmitted intensity, as in [15]. If the time of flight was a monotonic function, the statistical analysis would be simplified. The sum in Eq. (18) would be removed and we would be left with the standard formula to transform probability density functions. The predicted distributions are strongly dependent on the type of model used to describe the optical forces, and the ray optics model generally predicts longer t_{TOF}. From Eq. (18), for some values the PDFs diverge due to turning points in the $g(r)$ function ($g'(r) = 0$), which is the reason for the sharp peaks in the distributions. Although the PDF itself diverges, the probability of measuring a time of flight within a certain range, represented by the area underneath the PDF over that range, does not. Due to the oscillations present in the Lorenz-Mie time of flight function, there are several values of radii for which $g'(r) = 0$, this creates a multi-peak distribution in the Lorenz-Mie PDF (Fig. 6(b)). To overlay the PDFs with the data and to provide a comparison of fitting quality, a minimizing algorithm is employed which first discretizes a modified PDF distribution, given by $f^{\text{overlay}}_{t_{TOF}}(t_p) = f_{t_{TOF}}(At_p - B)$ where the parameters A and B govern the stretch and translation of the PDF along the t_P axis, respectively. The discretization

Optics EXPRESS

of $f_{t_{TOF}}^{\text{overlay}}(t_p)$ is performed by generating a large number of simulated data points and using a binning equivalent to that performed on experimental data. To compare each model with the data, we minimise the parameter Δ through the optimization of A and B:

$$\Delta(A,B) = \sum_{i=1}^{N} \frac{\left(h_{\text{exp}}(i) - h_{\text{PDF}}(i;A,B)\right)^2}{h_{\text{PDF}}(i;A,B)}, \tag{19}$$

with $N = 8$ the number of bins considered according to Sturge's rule [41], $h_{\text{exp}}(i)$ indicating the number of events falling in the $i-$th bin and $h_{\text{PDF}}(i;A,B)$ being the predicted number of events in the same bin. From this analysis, $\Delta_{\text{ro}} = 10.5$ counts for the ray optics treatment and $\Delta_{\text{Mie}} = 5.7$ counts for the Lorenz-Mie theory, which shows that the Lorenz-Mie model predicts a distribution shape that is more consistent with our data. The PDF distributions in Fig. 6(b) and (d) are plotted in blue using the optimized values of A and B, with the experimental data overlayed in pink.

One limitation here is due to the assumption that the coupling to the fundamental mode of the HC-PCF is perfect. It is actually expected that around 10% of power couples to higher order modes [8]. This means that instead of following a straight-line trajectory, the particle follows a sine-like trajectory, caused by the intermodal beating pattern inside the fiber. Small oscillations in the transverse direction have 1.35 μm predicted amplitude, leading to a corresponding error which might affect the translation of the predicted distribution along the t_p axis.

5. Conclusion

In conclusion, a method for optical force calculation has been developed and applied for microspheres in HC-PCFs, which is not limited to specific system dimension ranges. It is particularly useful at the edge of the ray optics regime, which is frequently used in HC-PCF-microparticle experiments. Measurements of the time of flight of silica microspheres launched along HC-PCFs evidence that this method is more suitable than ray optics for describing the optical forces with typical experimental parameters. The model offers an accurate and practicable way to predict force behaviour in these systems, and it can also be applied to a variety of optical configurations, such as dual beam standing wave traps, suitable for nanospheres, or intermodal beating traps [8,9]. As the excitation of Mie resonances depends both on the size parameter of the microspheres and on the polarization and amplitude profiles of the beams propagating in the HC-PCF, features predicted by our analysis would allow for the possibility of finely tuning optical trap parameters, with relevant applications including particle sorting and inspection, pollution monitoring, and remote temperature sensing architectures.

Funding. H2020 Marie Skłodowska-Curie Actions (813367).

Disclosures. The authors declare that there are no conflicts of interest related to this article.

Data availability. Data underlying the results presented in this paper are not publicly available at this time but may be obtained from the authors upon reasonable request.

References

1. M. J. Renn, D. Montgomery, O. Vdovin, D. Z. Anderson, C. E. Wieman, and E. A. Cornell, "Laser-guided atoms in hollow-core optical fibers," Phys. Rev. Lett. **75**(18), 3253–3256 (1995).
2. M. J. Renn, R. Pastel, and H. J. Lewandowski, "Laser guidance and trapping of mesoscale particles in hollow-core optical fibers," Phys. Rev. Lett. **82**(7), 1574–1577 (1999).
3. J. Dai and J. A. Harrington, "High-peak-power, pulsed CO_2 laser light delivery by hollow glass waveguides," Appl. Opt. **36**(21), 5072–5077 (1997).
4. R. F. Cregan, B. J. Mangan, J. C. Knight, T. A. Birks, P. S. J. Russell, P. J. Roberts, and D. C. Allan, "Single-mode photonic band gap guidance of light in air," Science **285**(5433), 1537–1539 (1999).
5. F. Benabid, J. Knight, G. Antonopoulos, and P. S. J. Russell, "Stimulated Raman scattering in hydrogen-filled hollow-core photonic crystal fiber," Science **298**(5592), 399–402 (2002).
6. F. Amrani, J. H. Osório, F. Delahaye, F. Giovanardi, L. Vincetti, B. Debord, F. Gérôme, and F. Benabid, "Low-loss single-mode hybrid-lattice hollow-core photonic-crystal fibre," Light: Sci. Appl. **10**(1), 7 (2021).

Optics EXPRESS

7. T. G. Euser, M. K. Garbos, J. S. Y. Chen, and P. S. J. Russell, "Precise balancing of viscous and radiation forces on a particle in liquid-filled photonic bandgap fiber," Opt. Lett. **34**(23), 3674–3676 (2009).
8. D. Grass, J. Fesel, S. Hofer, N. Kiesel, and M. Aspelmeyer, "Optical trapping and control of nanoparticles inside evacuated hollow core photonic crystal fibers," Appl. Phys. Lett. **108**(22), 221103 (2016).
9. O. A. Schmidt, T. G. Euser, and P. S. J. Russell, "Mode-based microparticle conveyor belt in air-filled hollow-core photonic crystal fiber," Opt. Express **21**(24), 29383–29391 (2013).
10. D. S. Bykov, S. Xie, R. Zeltner, A. Machnev, G. Wong, T. G. Euser, and P. S. J. Russell, "Long-range optical trapping and binding of microparticles in hollow-core photonic crystal fibre," Light: Sci. Appl. **7**(1), 22 (2018).
11. H. Su, N. Li, C. Wang, W. Li, Z. Fu, and H. Hu, "Optical rotation conveyor belt based on a polarization-maintaining hollow-core photonic crystal fiber," Opt. Rev. **27**(6), 561–567 (2020).
12. M. K. Garbos, T. G. Euser, O. A. Schmidt, S. Unterkofler, and P. S. J. Russell, "Doppler velocimetry on microparticles trapped and propelled by laser light in liquid-filled photonic crystal fiber," Opt. Lett. **36**(11), 2020–2022 (2011).
13. D. S. Bykov, O. A. Schmidt, T. G. Euser, and P. S. J. Russell, "Flying particle sensors in hollow-core photonic crystal fibre," Nat. Photonics **9**(7), 461–465 (2015).
14. T. Biswas, A. Mohamed, and M. Bhattacharya, "Rotating levitated nanoparticle sensors in a hollow-core photonic crystal fiber," J. Opt. Soc. Am. B **37**(6), 1598–1605 (2020).
15. A. Sharma, S. Xie, R. Zeltner, and P. S. J. Russell, "On-the-fly particle metrology in hollow-core photonic crystal fibre," Opt. Express **27**(24), 34496–34504 (2019).
16. D. Tzarouchis and A. Sihvola, "Light scattering by a dielectric sphere: Perspectives on the mie resonances," Appl. Sci. **8**(2), 184 (2018).
17. B. R. Johnson, "Theory of morphology-dependent resonances: shape resonances and width formulas," J. Opt. Soc. Am. A **10**(2), 343–352 (1993).
18. A. Neves, W. Lopes-moreira, A. Fontes, T. Euser, and C. Cesar, "Toward waveguide-based optical chromatography," Front. Phys. **8**, 640 (2021).
19. I. Teraoka, S. Arnold, and F. Vollmer, "Perturbation approach to resonance shifts of whispering-gallery modes in a dielectric microsphere as a probe of a surrounding medium," J. Opt. Soc. Am. B **20**(9), 1937–1946 (2003).
20. L. L. Martín, C. Pérez-Rodríguez, P. Haro-González, and I. R. Martín, "Whispering gallery modes in a glass microsphere as a function of temperature," Opt. Express **19**(25), 25792–25798 (2011).
21. R. Zeltner, R. Pennetta, S. Xie, and P. S. J. Russell, "Flying particle microlaser and temperature sensor in hollow-core photonic crystal fiber," Opt. Lett. **43**(7), 1479–1482 (2018).
22. A. Ashkin, "Forces of a single-beam gradient laser trap on a dielectric sphere in the ray optics regime," Biophys. J. **61**(2), 569–582 (1992).
23. J. Stratton, *Electromagnetic Theory* (McGraw-Hill, 1941).
24. G. Gouesbet and G. Gréhan, *Generalized Lorenz-Mie Theories* (Springer International Publishing, 2017).
25. A. A. R. Neves and C. L. Cesar, "Analytical calculation of optical forces on spherical particles in optical tweezers: tutorial," J. Opt. Soc. Am. B **36**(6), 1525–1537 (2019).
26. J. D. Jackson, *Classical Electrodynamics*, 3rd ed. (Wiley, 1999).
27. A. J. Devaney and E. Wolf, "Multipole expansions and plane wave representations of the electromagnetic field," J. Math. Phys. **15**(2), 234–244 (1974).
28. C. Bohren and D. Huffman, *Absorption and Scattering of Light by Small Particles* (Wiley-VCH, 1998).
29. W. L. Moreira, A. A. R. Neves, M. K. Garbos, T. G. Euser, and C. L. Cesar, "Expansion of arbitrary electromagnetic fields in terms of vector spherical wave functions," Opt. Express **24**(3), 2370–2382 (2016).
30. M. Digonnet, H. K. Kim, G. Kino, and S. Fan, "Understanding air-core photonic-bandgap fibers: analogy to conventional fibers," J. Lightwave Technol. **23**(12), 4169–4177 (2005).
31. T. G. Euser, G. Whyte, M. Scharrer, J. S. Y. Chen, A. Abdolvand, J. Nold, C. F. Kaminski, and P. S. J. Russell, "Dynamic control of higher-order modes in hollow-core photonic crystal fibers," Opt. Express **16**(22), 17972–17981 (2008).
32. M. K. Garbos, T. G. Euser, and P. S. J. Russell, "Optofluidic immobility of particles trapped in liquid-filled hollow-core photonic crystal fiber," Opt. Express **19**(20), 19643–19652 (2011).
33. G. Roosen, "A theoretical and experimental study of the stable equilibrium positions of spheres levitated by two horizontal laser beams," Opt. Commun. **21**(1), 189–194 (1977).
34. P. Chýlek, J. T. Kiehl, and M. K. W. Ko, "Narrow resonance structure in the mie scattering characteristics," Appl. Opt. **17**(19), 3019–3021 (1978).
35. P. Waterman, "Matrix formulation of electromagnetic scattering," in *Proceedings of the IEEE*, vol. 53 (1965), pp. 805–812.
36. R. K. Chang and P. W. Barber, *Optical Effects Associated with Small Particles* (World Scientific, 1988).
37. X. Liu, J. Laegsgaard, and D. Turchinovich, "Highly-stable monolithic femtosecond yb-fiber laser system based on photonic crystal fibers," Opt. Express **18**(15), 15475–15483 (2010).
38. D. R. Burnham and D. McGloin, "Holographic optical trapping of aerosol droplets," Opt. Express **14**(9), 4175–4181 (2006).
39. S. B. Chen and X. Ye, "Faxen's Laws of a Composite Sphere under Creeping Flow Conditions," J. Colloid Interface Sci. **221**(1), 50–57 (2000).

Optics EXPRESS

40. H. Kobayashi, B. L. Mark, and W. Turin, *Probability, Random Processes, and Statistical Analysis: Applications to Communications, Signal Processing, Queueing Theory and Mathematical Finance* (Cambridge University, 2011).
41. H. A. Sturges, "The choice of a class interval," J. Am. Stat. Assoc. **21**(153), 65–66 (1926).